



**HAL**  
open science

## **Synthesis of 2D perovskite crystals via progressive transformation of quantum well thickness**

Jin Hou, Wenbin Li, Hao Zhang, Siraj Sidhik, Jared Fletcher, Isaac Metcalf, Surendra B. Anantharaman, Xinting Shuai, Anamika Mishra, Jean-Christophe Blancon, et al.

### ► To cite this version:

Jin Hou, Wenbin Li, Hao Zhang, Siraj Sidhik, Jared Fletcher, et al.. Synthesis of 2D perovskite crystals via progressive transformation of quantum well thickness. *Nature Synthesis*, 2023, 3 (2), pp.265-275. <10.1038/s44160-023-00422-3>. <hal-04262698>

**HAL Id: hal-04262698**

**<https://hal.science/hal-04262698v1>**

Submitted on 31 Oct 2023

**HAL** is a multi-disciplinary open access archive for the deposit and dissemination of scientific research documents, whether they are published or not. The documents may come from teaching and research institutions in France or abroad, or from public or private research centers.

L'archive ouverte pluridisciplinaire **HAL**, est destinée au dépôt et à la diffusion de documents scientifiques de niveau recherche, publiés ou non, émanant des établissements d'enseignement et de recherche français ou étrangers, des laboratoires publics ou privés.



HAL Authorization

# 1 **Deterministic synthesis of phase-pure 2D perovskite crystals via** 2 **progressive transformation of quantum well thickness**

3 Jin Hou<sup>1</sup>, Wenbin Li<sup>2,3</sup>, Hao Zhang<sup>2,3</sup>, Siraj Sidhik<sup>1</sup>, Isaac Metcalf<sup>1</sup>, Surendra B.  
4 Anantharaman<sup>4</sup>, Xinting Shuai,<sup>1</sup> Anamika Mishra,<sup>2</sup> Jean-Christophe Blancon<sup>2</sup>, Claudine  
5 Katan<sup>5</sup>, Deep Jariwala<sup>4</sup>, Jacky Even<sup>6</sup>, Mercouri G. Kanatzidis<sup>7</sup> and Aditya D. Mohite<sup>1,2\*</sup>

6 <sup>1</sup>Department of Materials Science and NanoEngineering, Rice University, Houston, Texas  
7 77005, USA.

8 <sup>2</sup>Department of Chemical and Biomolecular Engineering, Rice University, Houston, Texas  
9 77005, USA.

10 <sup>3</sup>Applied Physics Graduate Program, Smalley-Curl Institute, Rice University, Houston, TX,  
11 77005, USA.

12 <sup>4</sup>Department of Electrical and Systems Engineering, University of Pennsylvania,  
13 Philadelphia, PA 19104, USA.

14 <sup>5</sup>Univ Rennes, ENSCR, INSA Rennes, CNRS, ISCR (Institut des Sciences Chimiques de  
15 Rennes) - UMR 6226, F-35000 Rennes, France.

16 <sup>6</sup>Univ Rennes, INSA Rennes, CNRS, Institut FOTON - UMR 6082, 35708 Rennes, France.

17 <sup>7</sup>Department of Chemistry and Department of Materials Science and Engineering,  
18 Northwestern University, Evanston, Illinois 60208, USA.

19  
20 **Two-dimensional (2D) multilayered halide perovskites have emerged as a platform for**  
21 **understanding organic-inorganic interactions, tuning quantum confinement effects and**  
22 **realizing efficient and durable optoelectronic devices. However, a major bottleneck has been**  
23 **reproducibly producing 2D perovskite crystals with desired perovskite-layer thicknesses**  
24 **(quantum well thickness, also known as n values) greater than two with the existing crystal**  
25 **growth methods. Here, we demonstrate a novel method termed kinetically controlled space**  
26 **confinement (KCSC) for the deterministic growth of phase pure Ruddlesden-Popper (RP)**  
27 **and Dion-Jacobson (DJ) 2D perovskites. The phase-pure growth is achieved by progressively**  
28 **increasing the temperature (for a fixed time) or the crystallization time (fixed temperature),**  
29 **which allows for acute control of the crystallization kinetics. In-situ photoluminescence**  
30 **spectroscopy and imaging suggest that the controlled increase in n-value (from lower to**  
31 **higher values of n=4, 5, and 6) occurs due to intercalation of excess precursor ions. Based on**  
32 **data from 250 experimental runs, phase diagrams for both RP and DJ perovskites have been**  
33 **constructed to predict the growth of 2D phases with specific n-values, facilitating the**  
34 **production of 2D perovskite crystals with desired layer thickness.**

35

36 Two-dimensional halide perovskites (2D-HaP) have emerged as a new class of highly durable  
37 solution-processed organic-inorganic (hybrid) low-dimensional semiconductors.<sup>1-3</sup> They exhibit a  
38 unique combination of properties derived from four exciting classes of materials - quantum wells,<sup>4</sup>  
39 atomically thin 2D materials<sup>5</sup>, organic semiconductors<sup>6,7</sup>, and 3D-HaP perovskites<sup>8,9</sup>. The general  
40 chemical formula of 2D-HaP is  $(A')_m(A)_{n-1}M_nX_{3n+1}$  (where A' is a bulky organic cation, A is a  
41 small organic cation, M is a divalent metal, X is a halide, with  $m=2$  in Ruddlesden-Popper (RP)  
42 phases and  $m=1$  in Dion-Jacobson (DJ) phases, and  $n$  determines the thickness of the perovskite  
43 layer), which consists of alternate layers of organics  $(A')_m$  and hybrid  $(A)_{n-1}M_nX_{3n+1}$ , providing a  
44 perfect platform to engineer hybrid composites with attractive optoelectronic properties. There is  
45 growing consensus that their physical properties are dictated by the interaction between the organic  
46 cation and the inorganic framework, which presents a unique opportunity to understand and tailor  
47 their behaviors,<sup>10</sup> including, charge-carrier mobility,<sup>11,12</sup> nonlinear optical effects,<sup>13</sup> tunable light  
48 emission,<sup>14,15</sup> electron-phonon coupling,<sup>16</sup> ferroelectricity,<sup>17,18</sup> Rashba effect<sup>19</sup> and transfer of  
49 chirality.<sup>20</sup> However, most of these studies on 2D HaPs have been performed on lower  $n$ -values  
50 ( $n=1, 2$ ) largely due to difficulties in reproducibly growing higher  $n$ -value phase pure crystals and  
51 films ( $n>2$ )<sup>5,13,21-23</sup>. We hypothesize that the mixed phases (multiple  $n$ -values) largely arise from  
52 the lack of sufficient control of crystallization kinetics (temperature, time) using the classical  
53 synthesis (CS) method for the growth of 2D HaP crystals and powders. Briefly, the CS method  
54 used across the perovskite research community involves dissolving all precursors in a solvent at  
55 an elevated temperature (230 °C) to achieve a supersaturated solution, followed by rapid  
56 crystallization through fast cooling by removing the solution from the hot plate to the ambient.<sup>1-</sup>  
57 <sup>3,24</sup> Once the temperature reaches below a certain point where supersaturation is excessive,  
58 nucleation will dominate, which results in a large number of small crystals (a few micrometers in  
59 size) in a short period of time (5-10 minutes). The fast nucleation due to the fast-cooling (230 °C  
60 to 25 °C almost instantaneously) makes it challenging to control the rate of crystallization and can  
61 result in the heterogeneous growth of unwanted phases. Therefore, we hypothesize that decoupling  
62 the crystallization temperature and time would enable a much better control over the kinetics of  
63 growth, which is challenging to achieve using the CS method since there is limited freedom to  
64 control the temperature or time one at a time during the crystallization process. As a result,  
65 understanding the impact of the kinetic parameters on realizing phase pure 2D perovskites has  
66 been largely unexplored and systematic studies on the effect on tuning the temperature or time of

67 crystallization for a given stoichiometry are still missing. In addition to difficulties in achieving  
68 phase pure crystals using the CS method, the powder forms of 2D-HaP are limited by their small  
69 crystal sizes ( $\mu\text{m}$  to  $\text{mm}$  sizes), making it challenging to precisely analyze the intrinsic physical  
70 properties such as (i) Light-matter interactions;<sup>25-27</sup> (ii) Optical measurement and dielectric  
71 functions where large-area flat crystals are required;<sup>4</sup> (iii) Electron-phonon interactions, where  
72 carrier trapping and exciton dissociation at grain boundaries or edges can often lead to complicated  
73 spectra.<sup>28-30</sup>

74 Attempts to cultivate large 2D hybrid perovskite (HaP) crystals have been made by slowing  
75 down growth through increased crystallization temperature and dilution,<sup>31,32</sup> but with limited  
76 success in achieving higher  $n$ -values ( $n \geq 4$ ).<sup>1,24,30,33-35</sup> Hence, the traditional methods of acquiring  
77 high  $n$ -value crystals have involved either (i) separating  $n$ -pure crystallites from an  $n$ -mixed  
78 crystal<sup>24</sup> or (ii) making several synthesis attempts. Nonetheless, a direct and reliable technique for  
79 producing phase-pure high  $n$ -value crystals is imperative.

80 Here we demonstrate that by either prolonging the crystallization time at a constant  
81 temperature or adjusting the synthesis temperature at a constant crystallization time, the initial 2D-  
82 HaP crystal can transform from lower to higher  $n$ -values. This transformation was verified through  
83 in-situ absorbance and x-ray diffraction measurements. To control the crystallization kinetics, we  
84 confined the precursor solution's volume between two glass slides and mounted it on a hot plate to  
85 precisely regulate the heating and cooling rates. In-situ photoluminescence spectroscopy and  
86 imaging suggest that the transformation from a lower  $n$ -value to a higher  $n$ -value starts from the  
87 edges of the preformed crystals, eventually converting the entire crystal into higher- $n$  2D-HaP  
88 crystals. Based on the experimental data collected from the KCSC method, we created multi-  
89 parameter phase diagrams for both the RP and DJ 2D-HaP using machine learning. Finally, we  
90 show that the concept of isothermal control can be translated to the CS process used commonly  
91 across the research community to synthesize powders of 2D-HaP, which allows us to synthesize  
92 2D-HaPs from  $n=1-6$ . We believe that the direct and reproducible approach method we propose  
93 for obtaining phase-pure single crystals and powders can be applied to RP and DJ-based  
94 perovskites of varying compositions. This will allow for a broader investigation of the physical  
95 properties of these perovskites, which has been previously limited to those with  $n=1$  or  $2$ .

96 Furthermore, these studies may uncover new opportunities for technological applications beyond  
97 using these perovskites solely as passivation layers or additives in bulk 3D perovskite films.<sup>33,36</sup>

## 98 **1. Result and discussion**

### 99 **1.1 KCSC method and transformation**

100 The progressive transformation to high  $n$  is demonstrated via the KCSC method, which is  
101 illustrated in Fig. 1a. To observe the transformation phenomenon, we used a parent solution of low  
102  $n$ -value ( $n=3$ ) stoichiometry (mol ratio, Pb: MA: BA=4: 2.67: 1.71) of  $\text{BA}_2\text{MA}_{n-1}\text{Pb}_n\text{I}_{3n+1}$  to obtain  
103 large-area crystals of high  $n$ -values ( $n=4-6$ ) by tuning the crystallization temperature and time.  
104 First, same as in CS, all the precursors (PbO, Methylammonium chloride (MACl), and Butylamine  
105 (BA)) are dissolved and mixed in the hydroiodic acid with the concentration of 0.85 M (based on  
106 Pb) at 190 °C. To prevent supersaturation and promote gradual growth of crystals, the solution is  
107 diluted by a factor of two. The diluted solution is then sandwiched between two preheated glass  
108 substrates treated with UV-ozone and placed on a hotplate for annealing at varying temperatures.  
109 When the substrate is annealed between 55°C and 105°C, a large crystal grows gradually due to  
110 limited solvent evaporation at the substrate's edge. Annealing below 55°C or above 105°C is not  
111 recommended as evaporation is minimal or the solution boils off, respectively. At a relatively low  
112 temperature within this range, the resulting crystal's  $n$  value corresponds to the parent solution's  
113 stoichiometry. For instance, annealing a parent solution of RP with  $n=3$  stoichiometry below 76°C  
114 produces a crystal with an  $n$  value of 3. Conversely, annealing at a higher temperature between  
115 80°C and 105°C leads to the formation of higher  $n$  values such as  $n=4$  and 5 as the initial crystal.  
116 If the temperature is kept constant and the crystal is monitored over time, the initial  $n$  value will  
117 transform into higher  $n$  values, regardless of the starting  $n$ -value.

118 We performed in-situ optical absorbance and X-ray spectroscopy measurements on the RP 2D-  
119 HaP crystal fabricated by the KCSC method using a parent solution with the stoichiometry of  $n=3$ ,  
120 where we tuned the temperature and time separately. For the time-dependent experiment, we  
121 increased the time of crystallization at a fixed temperature. For the temperature-dependent  
122 experiment, we varied the temperature of synthesis for a fixed crystallization time. Figure 1b  
123 illustrates the evolution of optical absorption as a function of temperature (ranging from 60-100 °C)  
124 for a fixed time of 7 hours using the same  $n=3$  stoichiometry parent solution. At low temperatures

125 (60-66 °C), we observed the formation of the n=3 crystal, which was identified based on the  
126 exciton absorption peak at 2.04 eV and also validated by comparison with that of the n=3 single  
127 crystal.<sup>1,4</sup> However, as we increase the temperature further to 68-79 °C, we observe a new peak at  
128 1.92 eV, which is redshifted from the n=3 peak. When further increasing the temperature from  
129 80 °C to 100 °C, we observed yet another set of peaks emerge at 1.85 eV and 1.8 eV. Evaluation  
130 of the peak positions and their comparison with a single crystal of 2D-HaP fabricated using the  
131 classical method suggests that these peaks at 1.92 eV, 1.85 eV, and 1.8 eV corresponding to n=4,  
132 n=5, and n=6 respectively,<sup>1,4</sup> which were further validated using x-ray diffraction measurements  
133 as shown in Fig. 1c. Briefly, the n=3 crystal is formed at 60 °C indicated by the set of corresponding  
134 (0k0) peaks consistent with the n=3 single crystals previously synthesized<sup>1,4,24</sup>, which upon  
135 increasing the temperature to 80 °C, gives rise to (0k0) peaks of n=4 with a concomitant decrease  
136 in the intensity of the n=3 peaks. As we further increased the temperature to 100 °C, (0k0) peaks  
137 of n=5 appeared and dominated, with the decreasing of the n=4 peaks. The evolution from n=3 to  
138 n=4 and finally n=5 observed in x-ray diffraction measurements is consistent with the temperature-  
139 dependent absorption measurements.

140 We changed the duration of crystallization at a constant temperature of 75°C and monitored the  
141 growth of a single perovskite crystal after every one-hour interval. The absorbance spectra versus  
142 time for the KCSC method are displayed in Figure 1d. Initially, n=3 was formed within 4 hours,  
143 followed by n=4 after 5 hours, causing the original n=3 excitonic peak intensity to decrease.  
144 Heating the crystal further at 75°C resulted in its transformation to n=5 after 13 hours. However,  
145 the crystal did not quickly convert from n=5 upon continued annealing, which is expected since  
146 the n=6 compound is less thermodynamically favorable.<sup>24</sup> The optical absorbance measurements  
147 are further supported by time-dependent XRD measurement as shown in Fig. 1e, and Fig. S1,  
148 where a n=3 crystal slowly transforms to n=4 after 7 hours of growth and finally to n=5 after 13  
149 hours. These measurements clearly show that we can tune the n value progressively by controlling  
150 temp and time separately.

151 The lateral size of the crystal fabricated by the KCSC method is a few millimeters to centimeters  
152 depending on the growth time. The thickness of the crystals is around 500 nm, which was  
153 calibrated to the amount of solution (Fig. S2) and the top glass slide used to confine the solution

154 since the spacing between two substrates could be tuned by varying the pressure applied to the  
 155 apparatus.<sup>31</sup> XRD measurements suggest that the orientation of the crystals are along the stacking

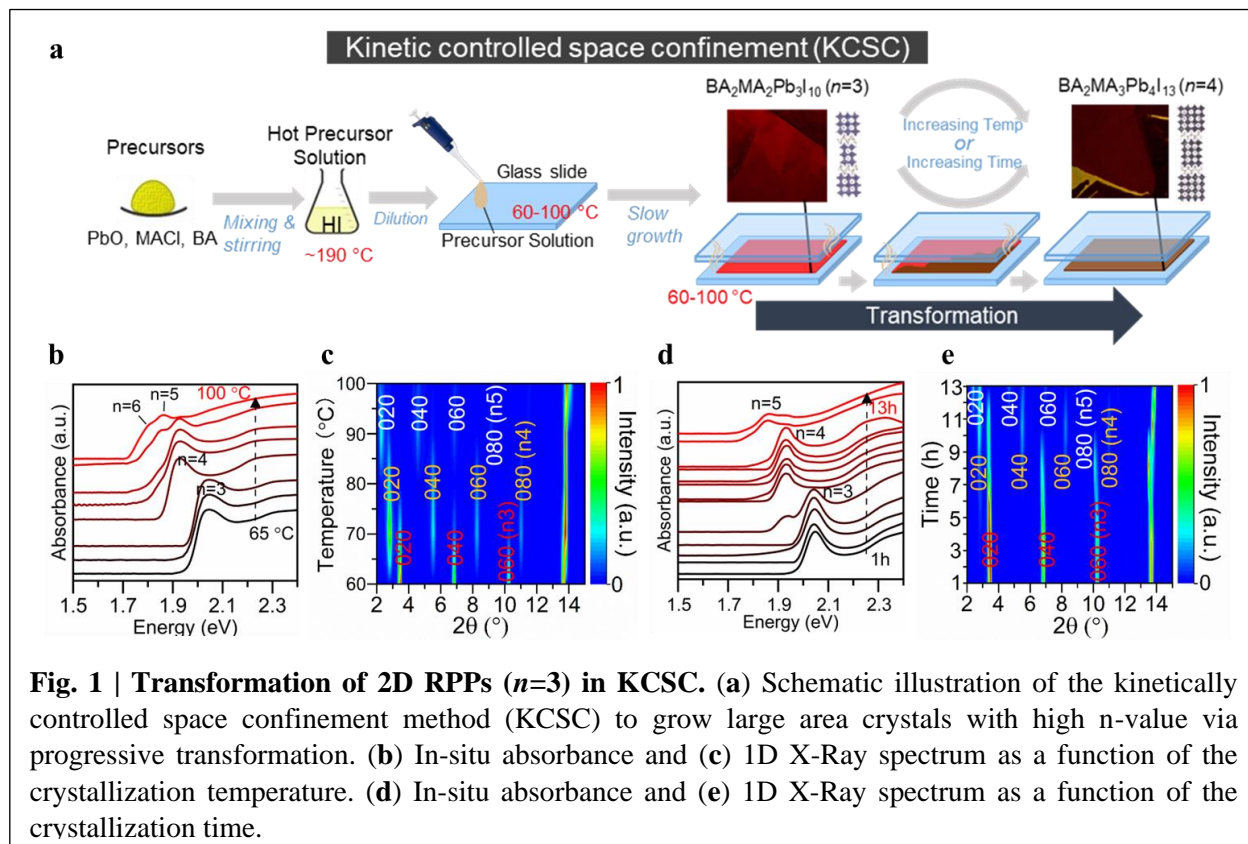


**Fig. 1 | Transformation of 2D RPPs ( $n=3$ ) in KCSC.** (a) Schematic illustration of the kinetically controlled space confinement method (KCSC) to grow large area crystals with high  $n$ -value via progressive transformation. (b) In-situ absorbance and (c) 1D X-Ray spectrum as a function of the crystallization temperature. (d) In-situ absorbance and (e) 1D X-Ray spectrum as a function of the crystallization time.

156 axis (or in-plane) as determined from the characteristic low angle ( $0k0$ ) reflections corresponding  
 157 to the lattice constants in the stacking direction (Figure S3) with no detectable signal of (111)  
 158 perovskite peak. Experimental Grazing incident wide-angle X-ray (GIWAX) measurements (Fig.  
 159 S4) match with simulated indexing of horizontally oriented 2D perovskite structure, indicating the  
 160 in-plane orientation of the perovskite layers.<sup>36</sup>

161 To rationalize the transformation in 2D HaP from a thermodynamics perspective, we calculate  
 162 the enthalpy of formation ( $\Delta H$ ) and the Gibbs free energy ( $\Delta G$ ) for the RP 2D-HaP crystal. The  
 163 enthalpy of transformation was calculated based on the reaction scheme given in table S1, where  
 164 the reactants are a specific  $n$ -value crystal,  $PbI_2$ , MAI while the product is the ( $n+1$ ) number  
 165 crystal (Fig. S5, Table S3-S5). Since  $\Delta G = \Delta H - T(\Delta S)$ , for the temperature-dependent  
 166 transformation, we have that  $\Delta G$  is mainly dependent on the  $\Delta H$  since the change of entropy  $\Delta S$  is  
 167 negligible<sup>24</sup>. The negative  $\Delta H$  value of -62.5 KJ/mol for the  $n=3$  to  $n=4$  transformation indicates  
 168 it is favorable. For the transformation of  $n=4$  to  $n=5$ , the  $\Delta H$  becomes more positive indicating a

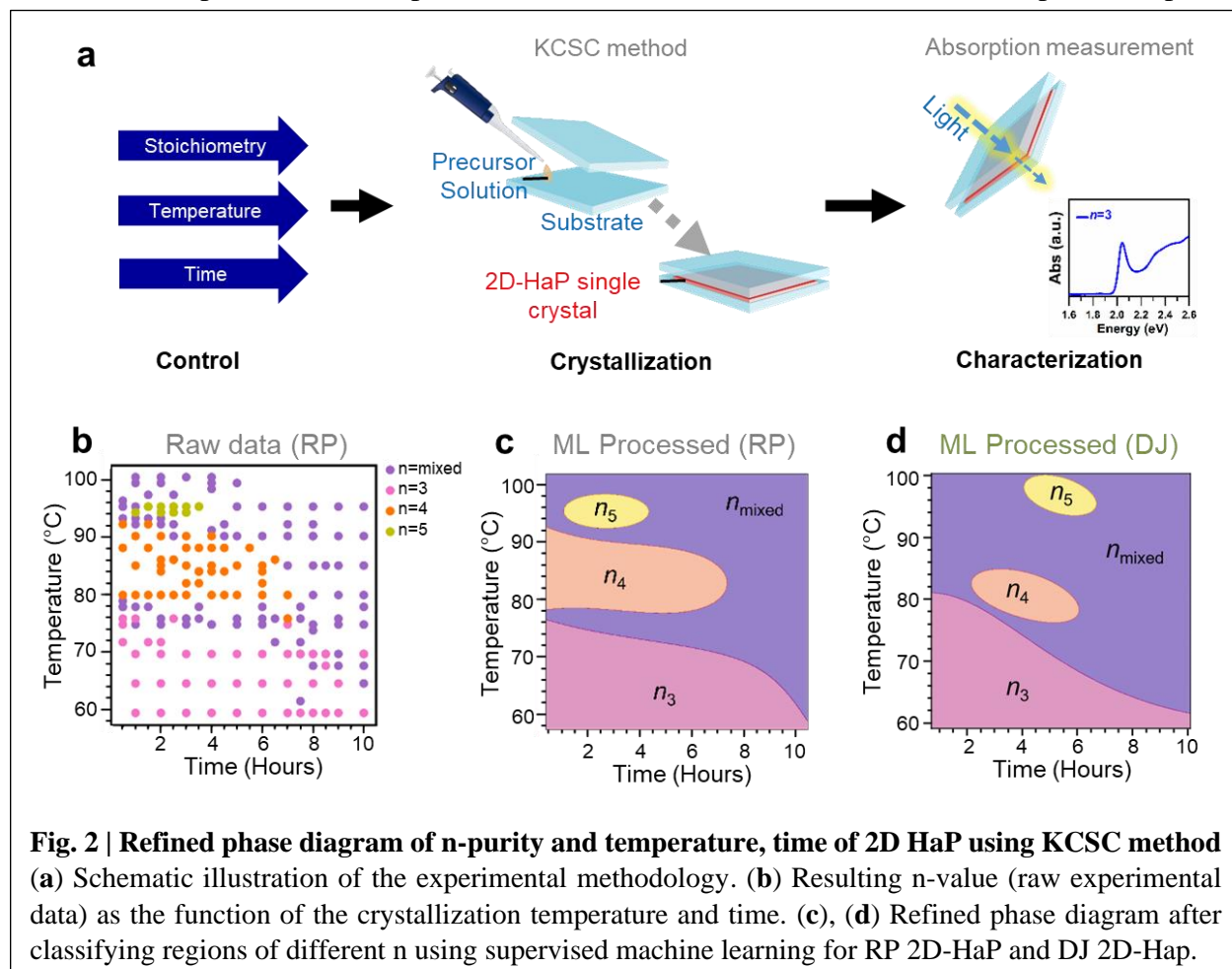
169 low probability of fabricating a phase pure 2D perovskite. Furthermore, the transformation from  
170  $n=5$  to  $n=6$  is extremely unfavorable because of the high enthalpy of transformation, equaling 149  
171 KJ/mol (Table S3). To overcome the large energy barrier, parent solutions of higher  $n$ -values  
172 ( $n=4,5$ ) were also tested with annealing at high temperature and long time. Higher  $n$ -value parent  
173 solutions facilitate the formation of higher  $n$ -value crystals compared to a  $n=3$  solution, but with  
174 decreasing reproducibility. For a  $n=4$  solution, a  $n=4$  crystal is formed at low temperature (below  
175  $76\text{ }^{\circ}\text{C}$ ), while at very high temperature ( $105\text{ }^{\circ}\text{C}$ ) with long annealing time (10 hours) it can form  
176  $n=6$  crystal (Fig. S6). For parent solution of  $n\geq 5$ , a specific  $n$ -value can not be obtained and 3D  
177 HaP is formed instead since it is more thermodynamically favorable than higher  $n$ -value ( $\Delta H_f: n=5$   
178  $< \text{MAPbI}_3(3\text{D}) < n=6$ ).<sup>24</sup>

## 179 **1.2 Building a multiparameter phase diagram**

180 To get a global view of the transformations and the relationship between phase purity,  
181 temperature and time, we designed and performed over 250 KCSC temperature and time-  
182 dependent syntheses for both RP and DJ. For DJ syntheses, we chose 3AMP as the organic cation  
183 spacer and used the same experimental methodology as used for RP as illustrated in Fig. 2a. Our  
184 approach consisted of four steps: (i) synthesizing the crystal using the same parent solution but  
185 with varying temperature and time; (ii) performing large area optical absorption measurements on  
186 the crystal, analyzing the excitonic absorption peak position to determine the  $n$ -value and; (iii)  
187 mapping the resulting  $n$ -value as the function of the temperature and time parameters; (iv)  
188 deploying machine learning (ML) analysis to refine the map and produce the phase diagram with  
189 smooth boundaries. Fig. 2b shows the results of the experiment of 2D-HaPs using  $n=3$   
190 stoichiometry parent solution, each data point represents one synthesis performed at a specific  
191 temperature during a given time. We classified them into four categories: the purple points indicate  
192  $n$ -mixed phases, the pink data points indicate  $n=3$ , orange indicates  $n=4$ , and yellow for  $n=5$ . The  
193  $n$ -mixed phases are defined if the crystal contains more than one  $n$  value indicated by the multiple  
194 excitonic absorption peaks. However, we find that in some regions there is a large variance of the  
195 phase pure and mixed-phase crystals. For example, when synthesizing large area  $n=3$  KCSC  
196 crystals at  $70\text{ }^{\circ}\text{C}$  and  $>8$  hours, the border between phase pure and mixed phases is blurred. Our

197 results show that at 70 °C and 9 hours, the KCSC synthesis produces a mixed phase (Fig. 2b).  
 198 However, at the same temperature but 10 hours, the sample is phase-pure  $n=3$ . To alleviate the  
 199 uncertainty in these boundaries, we used supervised machine learning (ML) to statistically classify  
 200 regions of pure phase vs mixed phase and to formulate a phase diagram (Fig. 2c). Specifically, we  
 201 deployed a support vector machine classifier to find the most optimal hyperplane, which can  
 202 separate the 2 classes, for this example  $n=3$  and the mixed phase. Details of the ML method can  
 203 be found in SI section 1.2.

204 For the RP type (Fig.2b), the crystals are phase-pure  $n=3$  irrespective of the annealing time  
 205 below 60 °C. As we slightly increase temperature (65 °C) the synthesized crystal at short annealing  
 206 times are still phase pure, but at longer annealing times the crystal becomes a mixture of phases  
 207 ( $n=3$  and  $n=4$ ). This indicates a fixed temperature higher than 65 °C is needed to trigger the  
 208 transformation. At a fixed temperature of 77 °C, the phase diagram shows that at all times the  
 209 KCSC method produces mixed phases. From 78 °C to 92 °C, the KCSC method produced phase



210 pure n =4 RP 2D-HaP right from the start of the annealing, which indicates that higher temperature  
211 will facilitate the formation of a higher n-value crystal, which is consistent with our  
212 thermodynamics calculations. As we increase the annealing time, the pure n=4 crystal also  
213 transforms into an n-mixed crystal because of intercalation. The pure n=5 crystal was acquired  
214 from a few conditions at higher temperatures (95 °C) but a relatively short time window. The phase  
215 diagram indicates that the temperature for isothermal transformations, determines the initial n-  
216 value and time controls the rate of the transformation.

217 Next, we investigate the DJ 2D-HaP using the same approach. As shown in fig. 2c, an ML-  
218 assisted mapping of crystals yielded by the KCSC method using 3-(aminomethyl) piperidinium  
219 (3AMP) DJ n=3 solution is plotted. By tuning the temperature and time of crystallization, the same  
220 parent n=3 solution formed crystals from n=3 to n=5 with high purity. The mapping of DJ 2D-HaP  
221 shows a similar trend compared to RP 2D-HaP, where the n-value increases as temperature and  
222 time of crystallization increase. The chances of synthesizing phase-pure crystal decrease with  
223 increasing n-value, which is demonstrated by the area decrease of the region area of ascendant-n  
224 in the map. Nonetheless, one difference between the RP and DJ phase diagram is: For DJ  
225 perovskites, the formation of higher n-values (n=4 and n=5) requires higher temperatures and  
226 longer times. This is attributed to the smaller interlayer spacing of DJ and additional interlayer  
227 interaction, limiting the precursor diffusion or the proposed intercalation mechanism (vide  
228 infra).<sup>2,27,37</sup> In summary, the concept of isothermal control demonstrated for both RP and DJ 2D-  
229 HaP series suggests it is generally applicable to all the 2D-HaPs.

### 230 **1.3 Mechanism of transformation**

231 To understand how the 2D-HaPs transform, we considered several possible pathways. Firstly,  
232 we looked at the concentration of the precursor solution and whether the loss of certain organic  
233 cations (Butyl Ammonium or aminomethyl pyridinium) during growth at high temperature could  
234 cause a change in concentration and thus a change in n value. Secondly, we examined whether the  
235 dissolution of lower n-value crystals and recrystallization of higher n-value crystals could  
236 contribute to the transformation. Thirdly, we considered the possibility that larger A' cations (such  
237 as BA) could escape from the perovskite structure during the transformation from n=3 to n=4-6.  
238 Finally, we looked at the idea that intercalation of MA<sup>+</sup>, Pb<sup>2+</sup>, and I<sup>-</sup> from the crystal edges of the  
239 first formed 2D-HaP crystal could increase the perovskite-layer thickness. Initially, we explored

240 the possibility that the change in  $n$  value was due to the loss of organic spacer cations during the  
241 annealing process, which could alter the proportion of inorganic and organic components and thus  
242 change the stoichiometry to form higher  $n$ -values. To test this hypothesis, we conducted  
243 experiments on RP and DJ perovskites, which contain BA and AMP cations. The BA has a boiling  
244 point of 78 °C but AMP is at ~230 °C, which is much higher than our experimental temperature  
245 range (60 – 100 °C). The organic spacer would not likely escape faster than other cations ( $\text{MA}^+$ ,  
246  $\text{Pb}^{2+}$ , and I) from the solution, therefore we ruled out this possibility.

247 To test the second, third, and fourth potential-pathways, we set up an in-situ photoluminescence  
248 (PL) imaging and PL spectrum during the crystal growth process to visualize the transformation  
249 (Fig.3). The PL setup is shown in Fig. 3a, where we measured the emission of the 2D-HaP crystal  
250 by exciting the whole region using a mercury vapor lamp with a 532 nm short pass filter mount  
251 before the sample. This allowed us to photoexcite and image the photoluminescence from the  
252 crystal and collect spectrally resolved information during the transformation from low  $n$  to high  $n$   
253 value. The PL images were collected by adding a Semrock Razoredge 633nm long pass filter right  
254 before the CCD camera. The filter suppresses the emission from the RP  $n=3$  perovskite and allows  
255 for the detection of the  $n=4$  phase. Figure 3c (Fig. S7) illustrates the evolution of the 2D-HaP  
256 single crystal as a function of time at 77 °C, the dark red region is  $n=3$  and the brighter red region  
257 is  $n=4$ . After the  $n=3$  crystal forms, under continuous heating we observe the appearance of the  
258  $n=4$  at the edge of the  $n=3$  crystal, and then with time, the  $n=4$  area expands and gradually converts  
259 the whole  $n=3$  region to  $n=4$ . Simultaneously, we also probed the photoluminescence spectra as a  
260 function of the growth time as shown in Fig. 3b. The circle illustrated on the PL images (fig. 3c)  
261 is the probe region with a laser beam diameter of ~15  $\mu\text{m}$  under a 10x objective. The spectra show  
262 a progressive change in emission peak from 630 nm to 650 nm indicating an increase in layer  
263 thickness from  $n=3$  to  $n=4$  which agrees with our hypothesis. In addition, the photoluminescence  
264 spectra show no other emissions from different sites, which excludes the possibility of defects and  
265 third-phase impurities. Lastly, both PL imaging and PL spectra results indicate that the  
266 transformation occurs much faster at the edges than in the bulk. We also probed the PL spectra  
267 from the back side of the crystal and the identical  $n$  was observed (fig.3d), which excluded the  
268 possibility that transformation is from a high  $n$ -value crystal forming on top of a lower  $n$ -value to  
269 form vertically stacked heterostructures.

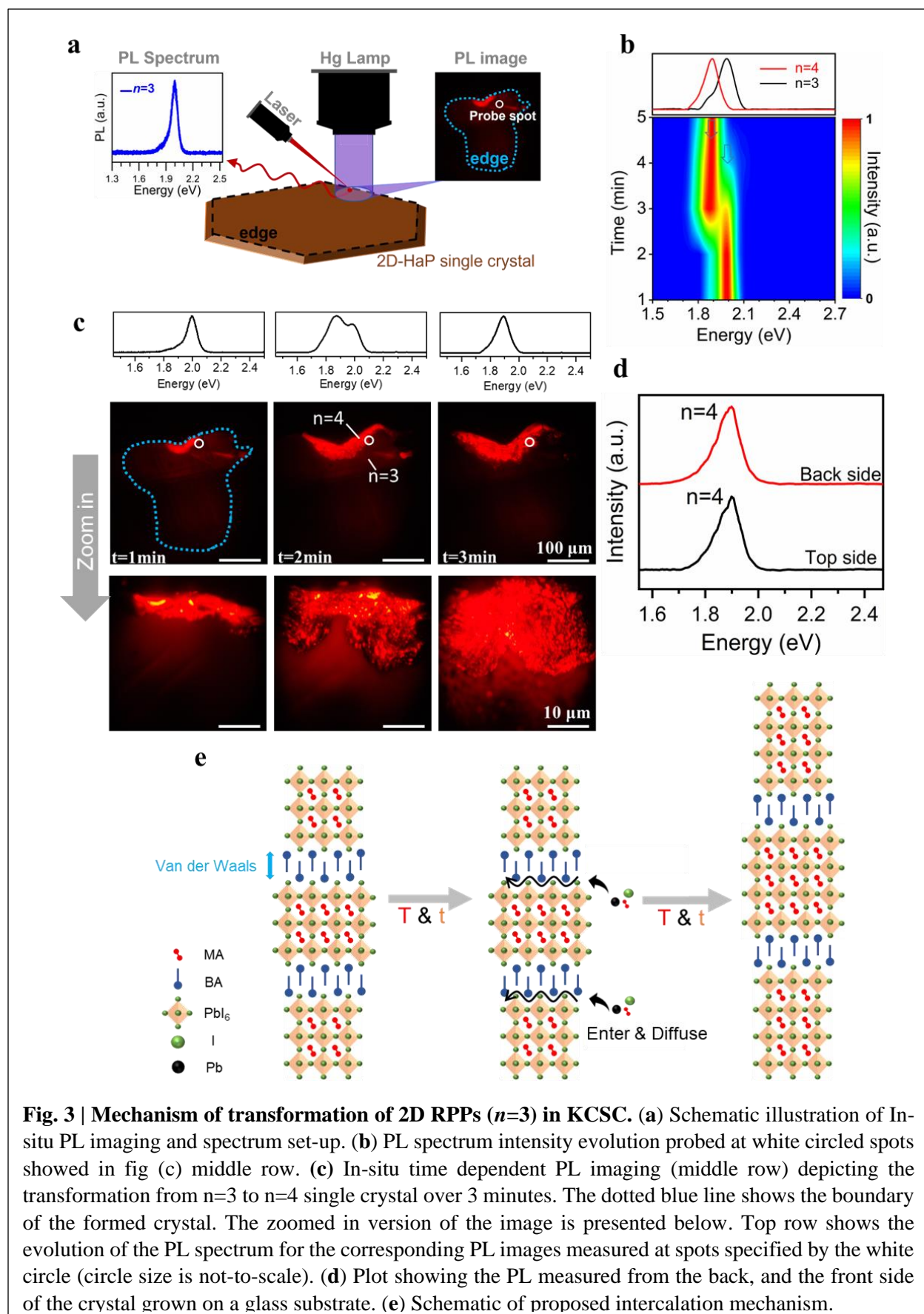


**Fig. 3 | Mechanism of transformation of 2D RPPs ( $n=3$ ) in KCSC.** (a) Schematic illustration of In-situ PL imaging and spectrum set-up. (b) PL spectrum intensity evolution probed at white circled spots showed in fig (c) middle row. (c) In-situ time dependent PL imaging (middle row) depicting the transformation from  $n=3$  to  $n=4$  single crystal over 3 minutes. The dotted blue line shows the boundary of the formed crystal. The zoomed in version of the image is presented below. Top row shows the evolution of the PL spectrum for the corresponding PL images measured at spots specified by the white circle (circle size is not-to-scale). (d) Plot showing the PL measured from the back, and the front side of the crystal grown on a glass substrate. (e) Schematic of proposed intercalation mechanism.

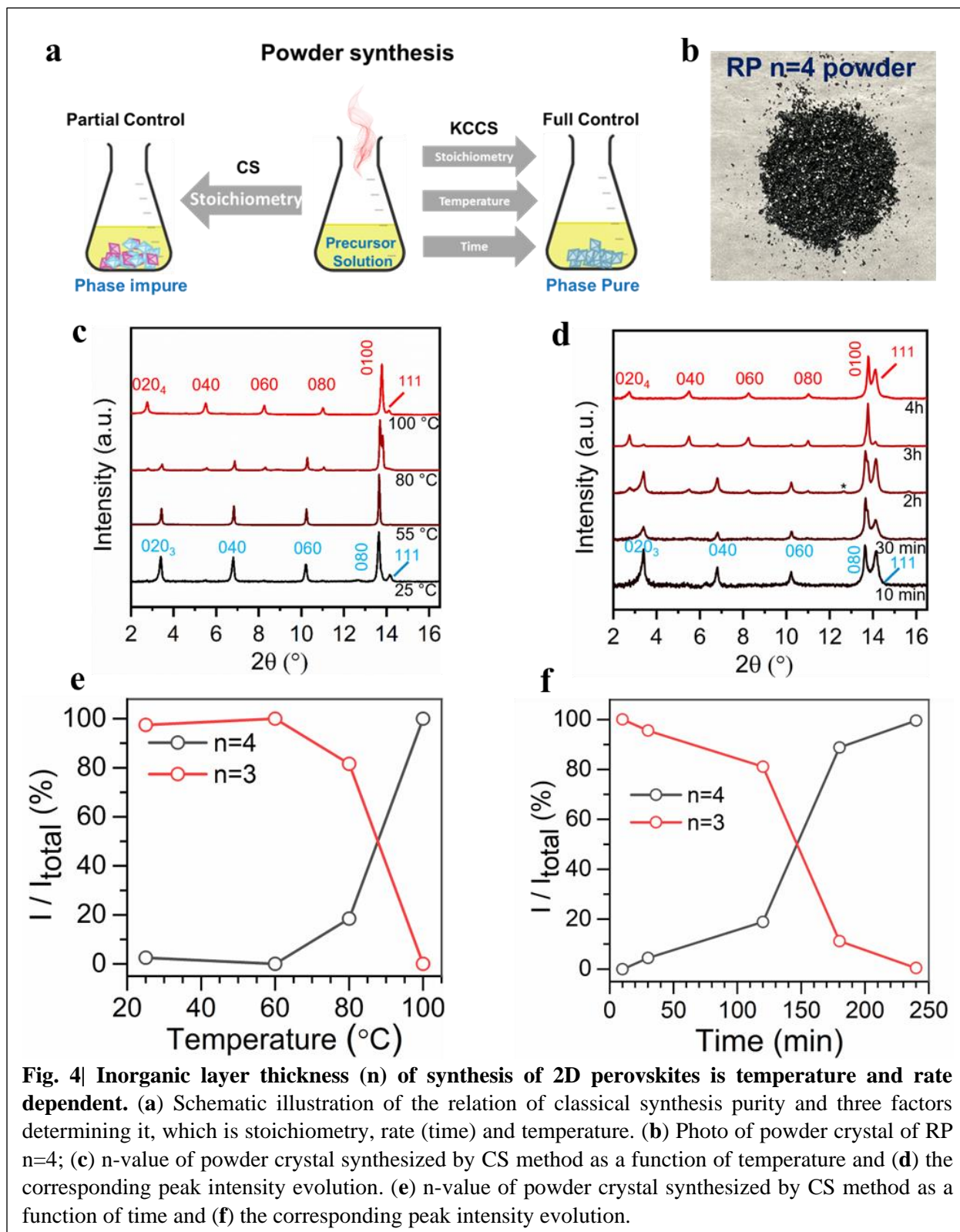
271 Therefore, the second mechanistic hypothesis is also excluded since the transformation occurs  
272 without dissolving the  $n=3$  and recrystallization of  $n=4$ . The third hypothesis was excluded after  
273 comparing our observations with a previous report by Fang et al.,<sup>38</sup> wherein a PL quenching (PL  
274 intensity decay) occurred after the 2-phenyl ethyl ammonium (another organic cation forming RP  
275 2D-HaP) left the perovskite framework due to laser-induced degradation. However, this is not the  
276 case observed in our PL experiments discussed in fig.3, where emissions from higher  $n$  emerged  
277 without a decrease in PL intensity.

278 Finally, we propose that the transformation is through an intercalation process, where small  
279 precursor ions, such as  $\text{MA}^+$ ,  $\text{Pb}^{2+}$ , and  $\text{I}^-$  penetrate the lattice from the edges of the 2D-HaP crystal  
280 and diffuse along the interface between the perovskite layers. These ions fill the voids of the  
281 corner-sharing  $\text{PbI}_6$  structure, forming additional linkages and integrate with the  $[\text{Pb}_n\text{I}_{3n+1}]$  lattice.  
282 This templating effect occurs because of the weak ionic interactions between the 2D inorganic  
283 octahedral sheets and the organic spacers. Figure 3e illustrates the proposed intercalation growth  
284 mechanism for the RP-HaP. Here, in the solution, the  $n=3$  perovskite forms first, which are shown  
285 by the stacking of 3 inorganic  $[\text{Pb}_n\text{I}_{3n+1}]^{(n+1)-}$  layers separated by the butylammonium organic  
286 spacer cations. Then over time, the organic MA, Pb, and I molecules diffuse through the edges of  
287 the  $n=3$  2D-HaP crystal and attach to the  $[\text{Pb}_n\text{I}_{3n+1}]$  structure. The intercalation process results in  
288 the increase of the layer thickness from  $n=3$  to  $n=4$  for the synthesized 2D-HaP. This mechanism  
289 also explains the observation that DJ HaP requires higher temperature and longer time for  
290 transformation because of the extra H-bond between spacer cation and octahedral in DJ HaP,  
291 slowing down the intercalation. Our results are consistent with previous reports that observe the  
292 intercalation of precursor ions into the lattice to form 2D-HaP and higher layer thickness 2D-HaP.  
293 For e. g., Guo et al.<sup>39</sup> proposed that extra halide additives ( $\text{K}^+$ ) would facilitate the intercalation  
294 of  $\text{PbBr}_6^{4-}$  octahedra into the lower- $n$   $\text{PEA}_2\text{FA}_{n-1}\text{Pb}_n\text{Br}_{3n+1}$  (PEA = phenylethylamine, FA =  
295 formamidine) to transform to higher  $n$  which is associated with Coulomb interaction.

#### 296 **1.4 Applying the KCSC to the classical method for batch-scale synthesis of 2D-HaPs powders**

297 While the KCSC method provides excellent control over phase pure, large area high  $n$ -value  
298 ( $n=1-6$ ) monocrystals of 2D-HaP, it is not scalable. As a result, with the goal of using the crystal  
299 transformation principle to achieve phase pure crystals in large quantities, we investigated the  
300 effects of controlling the temperature and time using a modified classical synthesis (CS) approach.

301 Figure 4a illustrates the CS method process, in which all the precursors are mixed in a concentrated  
 302 hydriodic acid (HI) at a specific stoichiometric ratio according to the target n-value. The solution  
 303 is heated to boiling and rapidly cooled to room temperature within 1 hour or even shorter period.



304 Small flakes with a typical lateral size of around 100  $\mu\text{m}$  were obtained. However, polycrystalline  
305 samples produced from this CS method often contain mixtures of different  $n$ -values. For example,  
306 Fig. S8a shows the X-ray diffraction pattern for 10 classically synthesized  $n=3$  RP samples, in  
307 which only 7 of the 10 syntheses achieved were phase-pure. The diffraction patterns of the  
308 unsuccessful synthesis show a consistent mixture of  $n=3$  and  $n=4$  phase (RP). Then we transposed  
309 the methodology developed in section 1.3 to the CS method. To ensure a uniform temperature  
310 across the precursor solution and also a prolonged cooling period, we immersed the reaction vial  
311 into an oil bath. The first parameter to tune is the temperature at which the boiling solution is left  
312 to crystallize. Instead of room temperature, we test a series of isothermal transformations, figure  
313 4c shows the powder X-ray diffraction of 2D-HaP powder crystals synthesized from 25  $^{\circ}\text{C}$  to  
314 100  $^{\circ}\text{C}$ . It shows a similar temperature dependent trend as observed in the KCSC method. Below  
315 60  $^{\circ}\text{C}$  the  $n=3$  forms but as the temperature is increased, the resulting powder becomes  $n=3$  and  
316  $n=4$  mixture at around 80  $^{\circ}\text{C}$  and finally pure  $n=4$  at 100 $^{\circ}\text{C}$ . However, as we showed in Fig. S8,  
317 compared to room temperature, crystallization at 55  $^{\circ}\text{C}$  has a higher probability to obtain pure  
318 crystal, which is consistent with the previous discussion in which fast precipitation of the 2D  
319 perovskite crystals results in mixed phases.<sup>40</sup> Our findings suggest that a temperature range of 40-  
320 55  $^{\circ}\text{C}$  is essential for the consistent and pure production of 2D-HaP. Within this range, we are able  
321 to slow down the crystallization process without inducing any changes caused by higher  
322 temperatures. This highlights that the temperature at which the solution is cooled is just as  
323 important as stoichiometry in the traditional synthesis method. Next, we also explored the impact  
324 of varying the total duration of the crystallization process. Figure 4d illustrates the X-ray  
325 diffraction patterns for various crystallization times with the temperature set to 90  $^{\circ}\text{C}$ . The results  
326 show a trend similar to the KCSC in which, as the time increases, the crystal transitions from  $n=3$   
327 into a mixture of  $n=3$  and  $n=4$  and finally phase pure  $n=4$  after 4 hours. Figure 4e and 4f are the  
328 intensity changes of the corresponding temperature and time-dependent XRD patterns, both of  
329 them show that  $n=3$  completely converts to  $n=4$ . The temperature and time-dependent observations  
330 we have made clearly demonstrate that stoichiometry is not the sole determinant of the  $n$ -value in  
331 powder 2D-HaP. Precise control over all three parameters is crucial for the production of a single  
332  $n$ -value 2D-HaP. As a result, we propose a new synthesis method called Kinetics-controlled classic  
333 synthesis (KCCS) that emphasizes the importance of the control of these parameters in powder  
334 synthesis.

335 **1.5 Phase pure n=1 to n=6 of RP and DJ 2D-HaPs**

336 Having established the importance of progressive transformation, we are able to grow phase pure  
337 single crystals ranging from n=1 to n=6 for both RP and DJ 2D-HaP. Figure 5a, 5b shows the  
338 absorption, and photoluminescence spectrum of KCSC produced n=1 to n=6 RP 2D-HaP single  
339 crystal. Each of the KCSC fabricated crystals exhibit a single narrow absorption peak decreasing  
340 from 2.42eV to 1.78eV as a function of n value (n=6 to n=1). The photoluminescence emission  
341 peak also follows this trend from 2.38eV to 1.77eV. This behavior is consistent with their quantum  
342 and dielectric confinement effects<sup>41</sup> and furthermore, indicates the phase purity of the fabricated  
343 crystals<sup>4</sup>. Both absorption and PL indicate the high purity of the crystal synthesized by our method.  
344 The absorption and photoluminescence of a control MAPbI<sub>3</sub> 3D-HaP are shown in the black curve

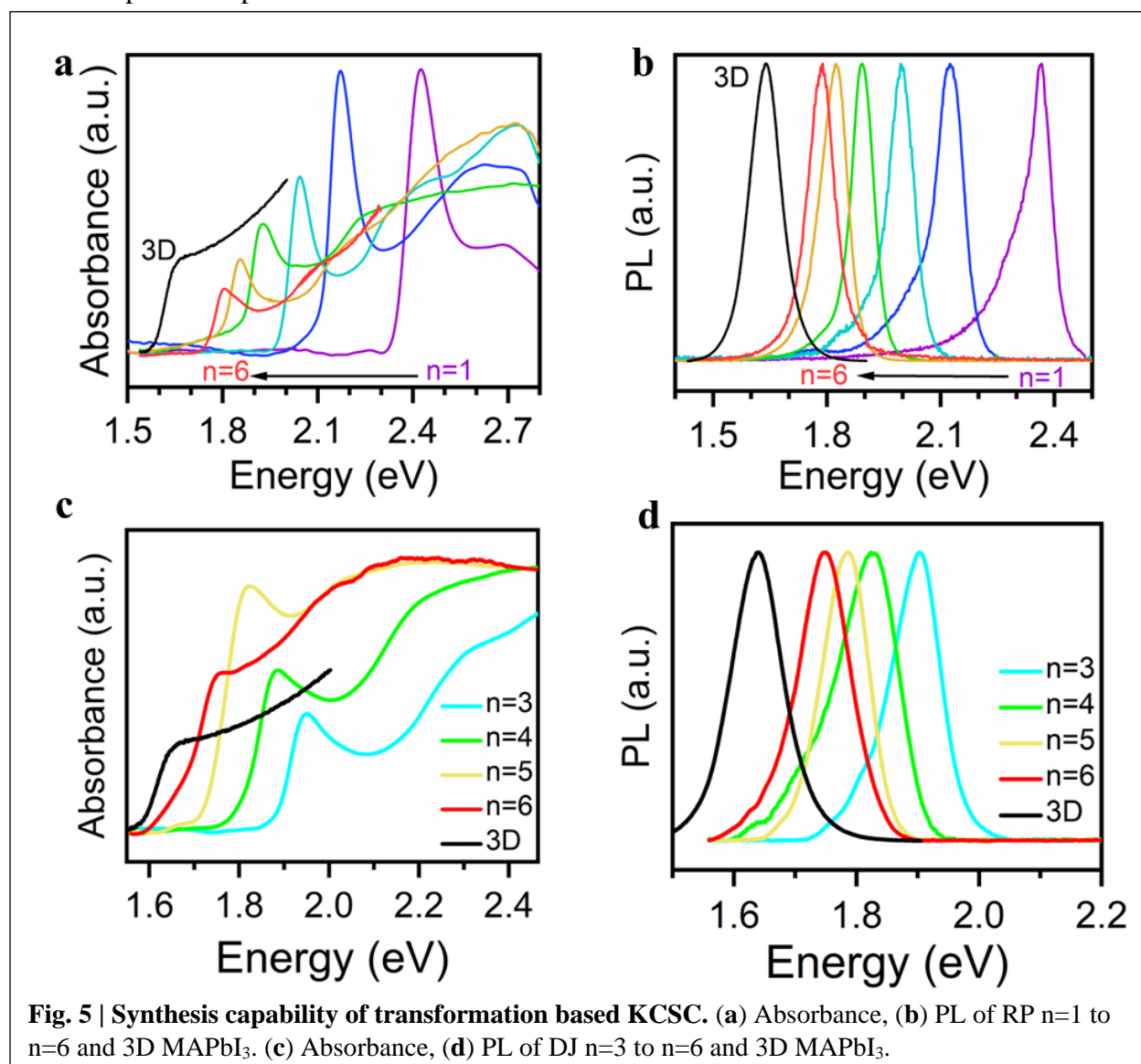


**Fig. 5 | Synthesis capability of transformation based KCSC. (a) Absorbance, (b) PL of RP n=1 to n=6 and 3D MAPbI<sub>3</sub>. (c) Absorbance, (d) PL of DJ n=3 to n=6 and 3D MAPbI<sub>3</sub>.**

345 on both plots. X-Ray diffraction of KCSC fabricated crystal (Fig. S9) also shows high purity.  
346 Figure 5c, d shows the absorption, and photoluminescence spectrum of KCSC produced n=3 to  
347 n=6 DJ 2D-HaP single crystal. Absorption (fig.5c) shows the 3AMP follows the general trend for  
348 2D-HaP where the band gap decreases as n increases (1.95eV for n=3, 1.88eV for n=4, 1.82eV for  
349 n=5, 1.75eV for n=6). Steady-state photoluminescence (PL) shows an identical trend with the band  
350 gaps (1.90eV for n=3, 1.82eV for n=4, 1.79eV for n=5, 1.75eV for n=6). Similar to the 2D-HaP  
351 synthesized from KCSC and transformation, the DJ 2D-HaP synthesized by the same approach is  
352 of high purity. The band gap of the DJ 3AMP series is smaller than the RP BA series, consistent  
353 with previous reports.<sup>2,37,42</sup> Transformation of the 4-(aminomethyl)piperidinium (4AMP) 2D-HaP  
354 is shown in Fig. S10.

## 355 2. Methods

### 356 2.1 Crystal synthesis

357 **2.1.1 Reagents:** PbO (99.9%), Methylammonium chloride (MACl, 99.0%), Butylamine (BA,  
358 99.0%), 4-(aminomethyl)piperidine (4AMP, 96%), hydroiodic acid (HI, 57 wt % in H<sub>2</sub>O, distilled,  
359 stabilized, 99.95%), hypophosphorous acid solution (H<sub>3</sub>PO<sub>2</sub>, 50 wt % in H<sub>2</sub>O) and diethyl ether  
360 ((C<sub>2</sub>H<sub>5</sub>)<sub>2</sub>O, 98%, contains 2% ethanol and ~10ppm BHT) were purchased from Sigma-Aldrich. 3-  
361 (aminomethyl)piperidine (3AMP, 98%) was purchased from TCI, Methylammonium iodide  
362 (MAI) were purchased from Greatcellsolar. All chemicals were used as received.

363

364 **2.1.2 Synthesis of (BA)<sub>2</sub>(MA)<sub>n-1</sub>Pb<sub>n</sub>I<sub>3n+1</sub> KCSC parent solution and powder crystal:** RP  
365 perovskites solution were synthesized by modifying the previously reported procedure<sup>1</sup>. For n =  
366 1, PbO powder (892.8 mg, 4mmol) was dissolved in a mixture of 57% w/w aqueous HI solution  
367 (4.0 mL, 30.4 mmol) and 50% aqueous H<sub>3</sub>PO<sub>2</sub> (1.0 mL, 9.1 mmol) at room temperature (25 °C)  
368 under constant magnetic stirring for 10 mins, which formed a bright yellow solution. In a separate  
369 beaker, n-CH<sub>3</sub>(CH<sub>2</sub>)<sub>3</sub>NH<sub>2</sub> (369.6 μL, 4 mmol) was neutralized with HI 57% w/w (2 mL, 15.2  
370 mmol) in an ice bath resulting in a clear yellow solution. The addition of the n-CH<sub>3</sub>(CH<sub>2</sub>)<sub>3</sub>NH<sub>3</sub>I  
371 solution to the PbI<sub>2</sub> solution initially produced orange precipitates, which were slowly dissolved  
372 under heating the combined solution to boiling. The solution was then diluted 3 times by aqueous  
373 HI solution. For higher n, PbO powder (892.8 mg, 4mmol) was dissolved in a mixture of 57% w/w  
374 aqueous HI solution (4.0 mL, 30.4 mmol) and 50% aqueous H<sub>3</sub>PO<sub>2</sub> (1mL, 9.1 mL) at room

375 temperature (25 °C) under constant magnetic stirring for 5 mins, which formed a bright yellow  
376 solution. Subsequent addition of solid CH<sub>3</sub>NH<sub>3</sub>Cl [135.2 mg, 2 mmol (n=2); 180 mg, 2.67 mmol  
377 (n=3); 202.8 mg, 3 mmol (n=4); 216 mg, 3.2 mmol (n=5)] at 230 °C initially caused the  
378 precipitation of black powders, which rapidly dissolved under stirring to afford a clear yellow  
379 solution. In a separate beaker, n-CH<sub>3</sub>(CH<sub>2</sub>)NH<sub>2</sub> [288 μL, 2.9 mmol (n=2); 170 μL, 1.71 mmol  
380 (n=3); 108.8 μL, 1.1 mmol (n=4); 88 μL, 0.89 mmol (n=5)] was neutralized with HI (2 mL, 15.2  
381 mmol) in an ice bath resulting in a clear yellow solution. After adding the n-CH<sub>3</sub>(CH<sub>2</sub>)<sub>3</sub>NH<sub>3</sub>I  
382 solution to the PbI<sub>2</sub> solution, the combined solution was kept at 230 °C, boiling for 10 mins. The  
383 solution was taken out and diluted 2 times with aqueous HI solution to afford a yellow clear  
384 solution, as the parent solution for the KCSC method.

385  
386 **2.1.3 Synthesis of (3AMP)(MA)<sub>2</sub>Pb<sub>3</sub>I<sub>10</sub> KCSC parent solution:** DJ perovskites solution were  
387 synthesized by modifying the stoichiometry reported in the 3-(aminomethyl)pyridinium (3AMPY)  
388 2D perovskites procedure.<sup>37</sup> The KCSC parent solution was diluted 3 times with aqueous HI  
389 solution and heated to 150 °C to ensure no crystals precipitated out before used to grow KCSC.

390  
391 **2.1.4 Growth of RP KCSC:** Glass (quartz, sapphire could also be used) was used as the substrate  
392 for the 2D perovskite growth. Glass substrates were cut into 1-inch\* 1-inch squares, cleaned in  
393 soap water, acetone, isopropanol by ultrasonication for 20 min each; then dried by argon. The  
394 substrates were transferred into a UV-Ozone cleaner, cleaned for 10 mins. The substrates were put  
395 on a hot plate, 10 μL of the parent solution was dropped onto the glass surface, another glass was  
396 put on top to fully cover the bottom glass and annealed. For n=1 large single crystal, n=1 parent  
397 solution is annealed at 70 °C for 6 hours. For n=2 large single crystal, n=2 parent solution is  
398 annealed at 70 °C for 6 hours. For n=3 large single crystal, n=3 parent solution is annealed at 60 °C  
399 for 5 hours. For n=4 large single crystal, n=3 parent solution is annealed at 80 °C for 6 hours. For  
400 n=5 large single crystal, n=3 parent solution is annealed at 95 °C for 4 hours. For n=6 large single  
401 crystal, n=4 parent solution is annealed at 105 °C for 10 hours. Then the top glass is removed, the  
402 crystal with the bottom glass is placed on spin coater, 40 μl \*3 of the diethyl ether was dropped  
403 instantly and spin coated at 3000 r.p.m for 30 seconds followed by heating for 15 minutes to  
404 remove all the residue parent solution.

405

406 **2.1.5 Growth of DJ KCSC:** For DJ phase, a growth procedure similar to BA was used with  
407 adjustment of temperature and time. For n=3 large single crystal, n=3 parent solution is annealed  
408 at 60 °C for 6 hours. For n=4 large single crystal, n=3 parent solution is annealed at 80 °C for 5  
409 hours. For n=5 large single crystal, n=3 parent solution is annealed at 96 °C for 6.5 hours. For n=6  
410 large single crystal, n=4 parent solution is annealed at 105 °C for 10 hours.

411

## 412 **2.2 X-ray diffraction measurements**

413 The measurements were conducted using a Rigaku Smartlab X-Ray diffractometer with Cu(K $\alpha$ )  
414 radiation ( $\lambda = 1.5406 \text{ \AA}$ ). For each KCSC sample, it was measured right after removing the top  
415 glass and washing the crystal, with a step of  $0.03^\circ$  and a speed of 3 degrees per minute. For the  
416 powder crystal, it dried in a vacuum oven at 65 °C overnight before measurement.

417

## 418 **2.3 Grazing incidence wide angle x-ray scattering (GIWAXS)**

419 The GIWAXS diffraction spectra used in this paper were high-resolution synchrotron patterns  
420 measured at 11-BM at the National Synchrotron Light Source-II (NSLS II). At beamline 11-BM,  
421 samples were placed on a robotic stage inside a vacuum chamber 6 (10<sup>-2</sup> torr) with the sample  
422 267mm away from a Pilatus 800K (Dectris) area detector. The photon energy was 13.5 keV, and  
423 the beam size was 200  $\mu\text{m} \times 50 \mu\text{m}$  (H  $\times$  V).

424

## 425 **2.4 In-situ absorbance measurements**

426 The optical absorbance measurements were conducted using a broad-band light source (Thorlabs  
427 Solis-3C) focused onto the sample with a 50  $\mu\text{m}$  beam size. The transmitted spectrum was collected  
428 by optical fiber and then sent to the spectrometer (Andor Kymera 328i) and CCD (Andor iDus  
429 416). The measurement was conducted on the KCSC apparatus without removing the top glass.

430

## 431 **2.5 In-situ PL imaging and spectrum measurements**

432 The in-situ PL imaging was conducted based on a lab-built widefield microscope using a Mercury  
433 light source (Olympus U-LH100HG) for illumination source which was loosely focused onto the  
434 sample on the hot plate. The PL was spectrally filtered by a long-pass filter (BLP01-647R,  
435 Semrock) to selectively monitor the emission from RP BA n=4 crystal, and the PL images were  
436 monitored as time lapses recorded by a microscope camera (AmScope MU500). The in-situ PL

437 spectrum was collected on the same area by focusing a 543.5nm Helium-Neon Laser onto a 15  $\mu$ m  
438 spot within the field of view of the PL image and was monitored by CCD spectrometer (Thorlabs  
439 CCS200). Both PL imaging and PL setup were interchangeable without repositioning the samples,  
440 allowing for spatially and spectrally-resolved in-situ PL tracing. Both measurements were  
441 conducted on the KCSC apparatus without removing the top glass.

442

## 443 References

- 444 (1) Stoumpos, C. C.; Cao, D. H.; Clark, D. J.; Young, J.; Rondinelli, J. M.; Jang, J. I.; Hupp, J. T.;  
445 Kanatzidis, M. G. Ruddlesden–Popper Hybrid Lead Iodide Perovskite 2D Homologous  
446 Semiconductors. *Chem. Mater.* **2016**, *28* (8), 2852–2867.  
447 <https://doi.org/10.1021/acs.chemmater.6b00847>.
- 448 (2) Mao, L.; Ke, W.; Pedesseau, L.; Wu, Y.; Katan, C.; Even, J.; Wasielewski, M. R.; Stoumpos, C.  
449 C.; Kanatzidis, M. G. Hybrid Dion–Jacobson 2D Lead Iodide Perovskites. *J. Am. Chem. Soc.*  
450 **2018**, *140* (10), 3775–3783. <https://doi.org/10.1021/jacs.8b00542>.
- 451 (3) Soe, C. M. M.; Stoumpos, C. C.; Kepenekian, M.; Traoré, B.; Tsai, H.; Nie, W.; Wang, B.; Katan,  
452 C.; Seshadri, R.; Mohite, A. D.; Even, J.; Marks, T. J.; Kanatzidis, M. G. New Type of 2D  
453 Perovskites with Alternating Cations in the Interlayer Space,  $(\text{C}(\text{NH}_2)_3)(\text{CH}_3\text{NH}_3)_n\text{Pb}_n\text{I}_{3n}$   
454  $_{+1}$ : Structure, Properties, and Photovoltaic Performance. *J. Am. Chem. Soc.* **2017**, *139* (45),  
455 16297–16309. <https://doi.org/10.1021/jacs.7b09096>.
- 456 (4) Song, B.; Hou, J.; Wang, H.; Sidhik, S.; Miao, J.; Gu, H.; Zhang, H.; Liu, S.; Fakhraai, Z.; Even,  
457 J.; Blancon, J.-C.; Mohite, A. D.; Jariwala, D. Determination of Dielectric Functions and Exciton  
458 Oscillator Strength of Two-Dimensional Hybrid Perovskites. *ACS Mater. Lett.* **2021**, *3* (1), 148–  
459 159. <https://doi.org/10.1021/acsmaterialslett.0c00505>.
- 460 (5) Dou, L.; Wong, A. B.; Yu, Y.; Lai, M.; Kornienko, N.; Eaton, S. W.; Fu, A.; Bischak, C. G.; Ma,  
461 J.; Ding, T.; Ginsberg, N. S.; Wang, L.-W.; Alivisatos, A. P.; Yang, P. Atomically Thin Two-  
462 Dimensional Organic-Inorganic Hybrid Perovskites. *Science* **2015**, *349* (6255), 1518–1521.  
463 <https://doi.org/10.1126/science.aac7660>.
- 464 (6) Bao, Z.; Dodabalapur, A.; Lovinger, A. J. Soluble and Processable Regioregular Poly (3-  
465 hexylthiophene) for Thin Film Field-effect Transistor Applications with High Mobility. *Appl.*  
466 *Phys. Lett.* **1996**, *69* (26), 4108–4110.
- 467 (7) Mannsfeld, S. C.; Tee, B. C.; Stoltenberg, R. M.; Chen, C. V.; Barman, S.; Muir, B. V.; Sokolov,  
468 A. N.; Reese, C.; Bao, Z. Highly Sensitive Flexible Pressure Sensors with Microstructured Rubber  
469 Dielectric Layers. *Nat. Mater.* **2010**, *9* (10), 859–864.
- 470 (8) Kim, H.-S.; Lee, C.-R.; Im, J.-H.; Lee, K.-B.; Moehl, T.; Marchioro, A.; Moon, S.-J.; Humphry-  
471 Baker, R.; Yum, J.-H.; Moser, J. E. Lead Iodide Perovskite Sensitized All-Solid-State Submicron  
472 Thin Film Mesoscopic Solar Cell with Efficiency Exceeding 9%. *Sci. Rep.* **2012**, *2* (1), 1–7.
- 473 (9) Burschka, J.; Pellet, N.; Moon, S.-J.; Humphry-Baker, R.; Gao, P.; Nazeeruddin, M. K.; Grätzel,  
474 M. Sequential Deposition as a Route to High-Performance Perovskite-Sensitized Solar Cells.  
475 *Nature* **2013**, *499* (7458), 316–319.
- 476 (10) Blancon, J.-C.; Even, J.; Stoumpos, Costas. C.; Kanatzidis, Mercouri. G.; Mohite, A. D.  
477 Semiconductor Physics of Organic–Inorganic 2D Halide Perovskites. *Nat. Nanotechnol.* **2020**, *15*  
478 (12), 969–985. <https://doi.org/10.1038/s41565-020-00811-1>.
- 479 (11) Ghosh, D.; Acharya, D.; Pedesseau, L.; Katan, C.; Even, J.; Tretiak, S.; Neukirch, A. J. Charge  
480 Carrier Dynamics in Two-Dimensional Hybrid Perovskites: Dion–Jacobson vs. Ruddlesden–  
481 Popper Phases. *J. Mater. Chem. A* **2020**, *8* (42), 22009–22022.  
482 <https://doi.org/10.1039/D0TA07205B>.

- 483 (12) Milot, R. L.; Sutton, R. J.; Eperon, G. E.; Haghighirad, A. A.; Martinez Hardigree, J.; Miranda, L.;  
484 Snaith, H. J.; Johnston, M. B.; Herz, L. M. Charge-Carrier Dynamics in 2D Hybrid Metal–Halide  
485 Perovskites. *Nano Lett.* **2016**, *16* (11), 7001–7007. <https://doi.org/10.1021/acs.nanolett.6b03114>.
- 486 (13) Li, P.; Chen, Y.; Yang, T.; Wang, Z.; Lin, H.; Xu, Y.; Li, L.; Mu, H.; Shivananju, B. N.; Zhang, Y.  
487 Two-Dimensional CH<sub>3</sub>NH<sub>3</sub>PbI<sub>3</sub> Perovskite Nanosheets for Ultrafast Pulsed Fiber Lasers. *ACS*  
488 *Appl. Mater. Interfaces* **2017**, *9* (14), 12759–12765.
- 489 (14) Xing, J.; Zhao, Y.; Askerka, M.; Quan, L. N.; Gong, X.; Zhao, W.; Zhao, J.; Tan, H.; Long, G.;  
490 Gao, L.; Yang, Z.; Voznyy, O.; Tang, J.; Lu, Z.-H.; Xiong, Q.; Sargent, E. H. Color-Stable Highly  
491 Luminescent Sky-Blue Perovskite Light-Emitting Diodes. *Nat. Commun.* **2018**, *9* (1), 3541.  
492 <https://doi.org/10.1038/s41467-018-05909-8>.
- 493 (15) Zhao, B.; Bai, S.; Kim, V.; Lamboll, R.; Shivanna, R.; Auras, F.; Richter, J. M.; Yang, L.; Dai, L.;  
494 Alsari, M.; She, X.-J.; Liang, L.; Zhang, J.; Lilliu, S.; Gao, P.; Snaith, H. J.; Wang, J.; Greenham,  
495 N. C.; Friend, R. H.; Di, D. High-Efficiency Perovskite–Polymer Bulk Heterostructure Light-  
496 Emitting Diodes. *Nat. Photonics* **2018**, *12* (12), 783–789. [https://doi.org/10.1038/s41566-018-](https://doi.org/10.1038/s41566-018-0283-4)  
497 0283-4.
- 498 (16) Gong, X.; Voznyy, O.; Jain, A.; Liu, W.; Sabatini, R.; Piontkowski, Z.; Walters, G.; Bappi, G.;  
499 Nokhrin, S.; Bushuyev, O. Electron–Phonon Interaction in Efficient Perovskite Blue Emitters. *Nat.*  
500 *Mater.* **2018**, *17* (6), 550–556.
- 501 (17) Shi, C.; Ye, L.; Gong, Z.-X.; Ma, J.-J.; Wang, Q.-W.; Jiang, J.-Y.; Hua, M.-M.; Wang, C.-F.; Yu,  
502 H.; Zhang, Y.; Ye, H.-Y. Two-Dimensional Organic–Inorganic Hybrid Rare-Earth Double  
503 Perovskite Ferroelectrics. *J. Am. Chem. Soc.* **2020**, *142* (1), 545–551.  
504 <https://doi.org/10.1021/jacs.9b11697>.
- 505 (18) Liu, Y.; Han, S.; Wang, J.; Ma, Y.; Guo, W.; Huang, X.-Y.; Luo, J.-H.; Hong, M.; Sun, Z. Spacer  
506 Cation Alloying of a Homoconformational Carboxylate *Trans* Isomer to Boost in-Plane  
507 Ferroelectricity in a 2D Hybrid Perovskite. *J. Am. Chem. Soc.* **2021**, *143* (4), 2130–2137.  
508 <https://doi.org/10.1021/jacs.0c12513>.
- 509 (19) Zhai, Y.; Baniya, S.; Zhang, C.; Li, J.; Haney, P.; Sheng, C.-X.; Ehrenfreund, E.; Vardeny, Z. V.  
510 Giant Rashba Splitting in 2D Organic-Inorganic Halide Perovskites Measured by Transient  
511 Spectroscopies. *Sci. Adv.* **2017**, *3* (7), e1700704. <https://doi.org/10.1126/sciadv.1700704>.
- 512 (20) Huang, P.-J.; Taniguchi, K.; Miyasaka, H. Bulk Photovoltaic Effect in a Pair of Chiral–Polar  
513 Layered Perovskite-Type Lead Iodides Altered by Chirality of Organic Cations. *J. Am. Chem. Soc.*  
514 **2019**, *141* (37), 14520–14523.
- 515 (21) Fieramosca, A.; De Marco, L.; Passoni, M.; Polimeno, L.; Rizzo, A.; Rosa, B. L. T.; Cruciani, G.;  
516 Dominici, L.; De Giorgi, M.; Gigli, G.; Andreani, L. C.; Gerace, D.; Ballarini, D.; Sanvitto, D.  
517 Tunable Out-of-Plane Excitons in 2D Single-Crystal Perovskites. *ACS Photonics* **2018**, *5* (10),  
518 4179–4185. <https://doi.org/10.1021/acsphotonics.8b00984>.
- 519 (22) Wang, J.; Li, J.; Lan, S.; Fang, C.; Shen, H.; Xiong, Q.; Li, D. Controllable Growth of Centimeter-  
520 Sized 2D Perovskite Heterostructures for Highly Narrow Dual-Band Photodetectors. *ACS Nano*  
521 **2019**, *12*.
- 522 (23) Wang, K.; Wu, C.; Yang, D.; Jiang, Y.; Priya, S. Quasi-Two-Dimensional Halide Perovskite  
523 Single Crystal Photodetector. *ACS Nano* **2018**, *12* (5), 4919–4929.  
524 <https://doi.org/10.1021/acsnano.8b01999>.
- 525 (24) Soe, C. M. M.; Nagabhushana, G. P.; Shivaramaiah, R.; Tsai, H.; Nie, W.; Blancon, J.-C.;  
526 Melkonyan, F.; Cao, D. H.; Traoré, B.; Pedesseau, L.; Kepenekian, M.; Katan, C.; Even, J.; Marks,  
527 T. J.; Navrotsky, A.; Mohite, A. D.; Stoumpos, C. C.; Kanatzidis, M. G. Structural and  
528 Thermodynamic Limits of Layer Thickness in 2D Halide Perovskites. *Proc. Natl. Acad. Sci.* **2019**,  
529 *116* (1), 58–66. <https://doi.org/10.1073/pnas.1811006115>.
- 530 (25) Singh, A.; Lynch, J.; Anantharaman, S. B.; Hou, J.; Singh, S.; Kim, G.; Mohite, A. D.; Singh, R.;  
531 Jariwala, D. Cavity-Enhanced Raman Scattering from 2D Hybrid Perovskites. *J. Phys. Chem. C*  
532 **2022**, *126* (27), 11158–11164. <https://doi.org/10.1021/acs.jpcc.2c01577>.

- 533 (26) Anantharaman, S. B.; Stevens, C. E.; Lynch, J.; Song, B.; Hou, J.; Zhang, H.; Jo, K.; Kumar, P.;  
534 Blancon, J.-C.; Mohite, A. D.; Hendrickson, J. R.; Jariwala, D. Self-Hybridized Polaritonic  
535 Emission from Layered Perovskites. *Nano Lett.* **2021**, *21* (14), 6245–6252.  
536 <https://doi.org/10.1021/acs.nanolett.1c02058>.
- 537 (27) Li, W.; Sidhik, S.; Traore, B.; Asadpour, R.; Hou, J.; Zhang, H.; Fehr, A.; Essman, J.; Wang, Y.;  
538 Hoffman, J. M.; Spanopoulos, I.; Crochet, J. J.; Tsai, E.; Strzalka, J.; Katan, C.; Alam, M. A.;  
539 Kanatzidis, M. G.; Even, J.; Blancon, J.-C.; Mohite, A. D. Light-Activated Interlayer Contraction  
540 in Two-Dimensional Perovskites for High-Efficiency Solar Cells. *Nat. Nanotechnol.* **2021**.  
541 <https://doi.org/10.1038/s41565-021-01010-2>.
- 542 (28) Zhang, H.; Li, W.; Essman, J.; Quarti, C.; Metcalf, I.; Chiang, W.-Y.; Sidhik, S.; Hou, J.; Fehr, A.;  
543 Attar, A. Ultrafast Relaxation of Lattice Distortion in Two-Dimensional Perovskites. *Nat. Phys.*  
544 **2023**, 1–6.
- 545 (29) Li, J.; Wang, H.; Li, D. Self-Trapped Excitons in Two-Dimensional Perovskites. *Front.*  
546 *Optoelectron.* **2020**, *13*, 225–234.
- 547 (30) Blancon, J.-C.; Tsai, H.; Nie, W.; Stoumpos, C. C.; Pedesseau, L.; Katan, C.; Kepenekian, M.;  
548 Soe, C. M. M.; Appavoo, K.; Sfeir, M. Y.; Tretiak, S.; Ajayan, P. M.; Kanatzidis, M. G.; Even, J.;  
549 Crochet, J. J.; Mohite, A. D. Extremely Efficient Internal Exciton Dissociation through Edge  
550 States in Layered 2D Perovskites. *Science* **2017**, *355* (6331), 1288–1292.  
551 <https://doi.org/10.1126/science.aal4211>.
- 552 (31) Chen, Y.-X.; Ge, Q.-Q.; Shi, Y.; Liu, J.; Xue, D.-J.; Ma, J.-Y.; Ding, J.; Yan, H.-J.; Hu, J.-S.; Wan,  
553 L.-J. General Space-Confined On-Substrate Fabrication of Thickness-Adjustable Hybrid  
554 Perovskite Single-Crystalline Thin Films. *J. Am. Chem. Soc.* **2016**, *138* (50), 16196–16199.  
555 <https://doi.org/10.1021/jacs.6b09388>.
- 556 (32) Leng, K.; Abdelwahab, I.; Verzhbitskiy, I.; Telychko, M.; Chu, L.; Fu, W.; Chi, X.; Guo, N.;  
557 Chen, Z.; Chen, Z. Molecularly Thin Two-Dimensional Hybrid Perovskites with Tunable  
558 Optoelectronic Properties Due to Reversible Surface Relaxation. *Nat. Mater.* **2018**, *17* (10), 908–  
559 914.
- 560 (33) Sidhik, S.; Wang, Y.; De Siena, M.; Asadpour, R.; Torma, A. J.; Terlier, T.; Ho, K.; Li, W.;  
561 Puthirath, A. B.; Shuai, X. Deterministic Fabrication of 3D/2D Perovskite Bilayer Stacks for  
562 Durable and Efficient Solar Cells. *Science* **2022**, *377* (6613), 1425–1430.
- 563 (34) Stoumpos, C. C.; Soe, C. M. M.; Tsai, H.; Nie, W.; Blancon, J.-C.; Cao, D. H.; Liu, F.; Traoré, B.;  
564 Katan, C.; Even, J. High Members of the 2D Ruddlesden-Popper Halide Perovskites: Synthesis,  
565 Optical Properties, and Solar Cells of (CH<sub>3</sub>(CH<sub>2</sub>)<sub>3</sub>NH<sub>3</sub>)<sub>2</sub>(CH<sub>3</sub>NH<sub>3</sub>)<sub>4</sub>Pb<sub>5</sub>I<sub>16</sub>. *Chem* **2017**, *2*  
566 (3), 427–440.
- 567 (35) Mao, L.; Kennard, R. M.; Traore, B.; Ke, W.; Katan, C.; Even, J.; Chabinye, M. L.; Stoumpos, C.  
568 C.; Kanatzidis, M. G. Seven-Layered 2D Hybrid Lead Iodide Perovskites. *Chem* **2019**, *5* (10),  
569 2593–2604. <https://doi.org/10.1016/j.chempr.2019.07.024>.
- 570 (36) Sidhik, S.; Li, W.; Samani, M. H. K.; Zhang, H.; Wang, Y.; Hoffman, J.; Fehr, A. K.; Wong, M.  
571 S.; Katan, C.; Even, J.; Marciel, A. B.; Kanatzidis, M. G.; Blancon, J.; Mohite, A. D. Memory  
572 Seeds Enable High Structural Phase Purity in 2D Perovskite Films for High-Efficiency Devices.  
573 *Adv. Mater.* **2021**, *33* (29), 2007176. <https://doi.org/10.1002/adma.202007176>.
- 574 (37) Li, X.; Ke, W.; Traoré, B.; Guo, P.; Hadar, I.; Kepenekian, M.; Even, J.; Katan, C.; Stoumpos, C.  
575 C.; Schaller, R. D.; Kanatzidis, M. G. Two-Dimensional Dion–Jacobson Hybrid Lead Iodide  
576 Perovskites with Aromatic Diammonium Cations. *J. Am. Chem. Soc.* **2019**, *141* (32), 12880–  
577 12890. <https://doi.org/10.1021/jacs.9b06398>.
- 578 (38) Fang, H.; Yang, J.; Tao, S.; Adjokatse, S.; Kamminga, M. E.; Ye, J.; Blake, G. R.; Even, J.; Loi,  
579 M. A. Unravelling Light-Induced Degradation of Layered Perovskite Crystals and Design of  
580 Efficient Encapsulation for Improved Photostability. *Adv. Funct. Mater.* **2018**, *28* (21), 1800305.
- 581 (39) Guo, Z.; Zhang, Y.; Wang, B.; Wang, L.; Zhou, N.; Qiu, Z.; Li, N.; Chen, Y.; Zhu, C.; Xie, H.;  
582 Song, T.; Song, L.; Xue, H.; Tao, S.; Chen, Q.; Xing, G.; Xiao, L.; Liu, Z.; Zhou, H. Promoting  
583 Energy Transfer via Manipulation of Crystallization Kinetics of Quasi-2D Perovskites for Efficient

- 584 Green Light-Emitting Diodes. *Adv. Mater.* **2021**, *33* (40), 2102246.  
585 <https://doi.org/10.1002/adma.202102246>.
- 586 (40) Li, X.; Hoffman, J. M.; Kanatzidis, M. G. The 2D Halide Perovskite Rulebook: How the Spacer  
587 Influences Everything from the Structure to Optoelectronic Device Efficiency. *Chem. Rev.* **2021**,  
588 *121* (4), 2230–2291. <https://doi.org/10.1021/acs.chemrev.0c01006>.
- 589 (41) Katan, C.; Mercier, N.; Even, J. Quantum and Dielectric Confinement Effects in Lower-  
590 Dimensional Hybrid Perovskite Semiconductors. *Chem. Rev.* **2019**, *119* (5), 3140–3192.
- 591 (42) Blancon, J.-C.; Stier, A. V.; Tsai, H.; Nie, W.; Stoumpos, C. C.; Traoré, B.; Pedesseau, L.;  
592 Kepenekian, M.; Katsutani, F.; Noe, G. T.; Kono, J.; Tretiak, S.; Crooker, S. A.; Katan, C.;  
593 Kanatzidis, M. G.; Crochet, J. J.; Even, J.; Mohite, A. D. Scaling Law for Excitons in 2D  
594 Perovskite Quantum Wells. *Nat. Commun.* **2018**, *9* (1), 2254. [https://doi.org/10.1038/s41467-018-](https://doi.org/10.1038/s41467-018-04659-x)  
595 [04659-x](https://doi.org/10.1038/s41467-018-04659-x).
- 596

597 **Acknowledgments:** The work at Rice University was supported by start-up funds under the  
598 molecular nanotechnology initiative and also the DOE-EERE 2022-1652 program. J.H.  
599 acknowledges the financial support from the China Scholarships Council (No. 202107990007).  
600 W.L. acknowledges the National Science Foundation Graduate Research Fellowship Program  
601 (This material is based upon work supported by the National Science Foundation Graduate  
602 Research Fellowship Program under grant no. NSF 20-587. Any opinions, findings and  
603 conclusions or recommendations expressed in this material are those of the author and do not  
604 necessarily reflect the views of the National Science Foundation). Work at Northwestern on  
605 perovskite solar cells is supported by the Office of Naval Research Grant N00014-20-1-2725). D.J.  
606 acknowledges primary support for this work by the U.S. Army Research Office under contract  
607 number W911NF-19-1-0109 and the Sloan Fellowship in Chemistry awarded by the Alfred P.  
608 Sloan Foundation. S.B.A. gratefully acknowledges the funding received from the Swiss National  
609 Science Foundation (SNSF) under the Early Postdoc Mobility grant (P2ELP2\_187977) for this  
610 work. J.E. acknowledges the financial support from the Institut Universitaire de France. The work  
611 at ISCR and Institut FOTON was performed with funding from the European Union’s Horizon  
612 2020 research and innovation program under grant agreement no. 861985 (PeroCUBE). This  
613 research used beamline 11-BM (CMS) of the NSLS-II and the Center for Functional  
614 Nanomaterials, both of which are US Department of Energy Office of Science User Facilities  
615 operated for the Department of Energy Office of Science by Brookhaven National Laboratory  
616 under contract no. DE-SC0012704. We thank Ruipeng Li and Esther Tsai for their assistance in  
617 performing experiments at beamline CMS. J.H. acknowledges the discussion with Prof. Ming  
618 Tang at Rice University and Prof. David Mitzi at Duke University.

619 **Author contributions:** J.H., J.-C.B. and A.D.M. conceived and designed the experiment. J.H. synthesized  
620 the perovskite single crystals with the help of S.S.. J.H. performed 1D-XRD measurements with the help  
621 of I.M., X.S. and A.M.. J.H. and H.Z. performed optical characterizations with the help of W.L. and S.B.A..  
622 J.H. performed the transformation experiment. W.L. performed the machine learning analysis. J.H.  
623 performed data analysis with guidance from C.K., D.J., J.-C.B., M.K., J.E., and A. D. M.. J.H. and W.L.  
624 wrote the manuscript with input from everyone. All authors read the manuscript and agree to its contents,  
625 and all data are reported in the main text and supplemental materials.

626 **Competing interests:** The authors declare no competing interests.